In-situ nanoscopic observations of dealloying-driven local corrosion from surface initiation to in-depth propagation

Kosari, A.; Zandbergen, H.; Tichelaar, F.; Visser, P.; Taheri, P.; Terryn, H.; Mol, J. M.C.

DOI
10.1016/j.corsci.2020.108912

Publication date
2020

Document Version
Final published version

Published in
Corrosion Science

Corrosion Science 177 (2020) 108912

Contents lists available at ScienceDirect

Corrosion Science

journal homepage: www.elsevier.com/locate/corsci

In-situ nanoscopic observations of dealloying-driven local corrosion from surface initiation to in-depth propagation

A. Kosari[a,*], H. Zandbergen[b], F. Tichelaar[b], P. Visser[c], P. Taheri[a], H. Terryn[d], J.M.C. Mol[a]

[a] Department of Materials Science and Engineering, Delft University of Technology, Mekelweg 2, 2628 CD Delft, the Netherlands
[b] Kavli Institute of Nanoscience, Delft University of Technology, Lorentzweg 1, 2628 CJ Delft, the Netherlands
[c] AkzoNobel, Rijksstraatweg 31, 2171 AJ Sassenheim, the Netherlands
[d] Department of Materials and Chemistry, Research Group Electrochemical and Surface Engineering (SURF), Vrije Universiteit Brussel, Pleinlaan 2, 1050 Brussels, Belgium

ARTICLE INFO

Keywords:
Aerospace aluminium alloys
In-situ liquid-phase TEM
Dealloying
Pitting corrosion
Copper redistribution

ABSTRACT

Dealloying is involved in materials science responsible for fabrication of nanoscale structures beneficially but for corrosion degradations detrimentally. Detailed understanding related to the latter is critical for designing corrosion-resistance alloys and dedicated inhibition systems. Thus, direct nanoscopic observations of nano-structural and compositional evolutions during the process are essential. Here using liquid phase-transmission electron microscopy (LP-TEM), for the first time, we show dynamic evolution of intricate site-specific local corrosion linked to intermetallic particles (IMPs) in aerospace aluminium alloys. To thoroughly probe degradation events, oxidation direction is controlled by purposefully masking thin specimens, allowing for observing top-view surface initiation to cross-sectional depth propagation of local degradations. Real-time capturing validated and supported by post-mortem examinations shows a dealloying-driven process that initiates at IMPs and penetrates into the depth of the alloy, establishing macroscopic corrosion pits. Besides, controversial mechanisms of noble-metal redistribution are finally elucidated.

1. Introduction

High-strength-to-weight ratio in aluminium alloys (AAs) is key to many transport industries like aerospace as it reduces dead-weight and energy consumption and beneficially increases loading capacity [1]. The main contributors to mechanical properties are nano-to microscale intermetallic compounds that are introduced to the aluminium-based systems by specific alloying followed by precipitation hardening processes [2–6] (Fig. 1 and Movie S1), but they are typically undesirably detrimental to the corrosion resistance [7]. Contemporary aerospace AAs benefit from a comprehensive metallurgical knowledge of tuning the microstructure towards desirable mechanical properties [8]. However, the detailed understanding to unambiguously describe how the engineered microstructures affect the corrosion properties is deficient to date. In particular, complicated site-specific local degradation events that predominantly take place at surface intermetallic particles (IMPs) dispersed in the AAs matrix eventually lead to progressive pitting and intergranular corrosion [9]. Furthermore, mechanical stress during imposed operating conditions may give rise to pit-to-crack transition, jeopardizing the integrity of the aluminium alloy structure [10]. Thus, the comprehensive primary knowledge of microstructure-affected corrosion properties is absolutely essential to designing and developing intrinsically corrosion resistant AAs.

Intermetallic compounds are electrochemically instable phases in aqueous environments and generally undergo dealloying due to selective removal of less-noble metal components towards formation of a nanoporous noble-metal morphology [11,12]. The dealloying process of binary or ternary systems is very complicated in terms of mechanism [13–16]. However, the mechanisms would be even more intricate when IMPs are confined in alloys as they can electrochemically interact (galvanic coupling) with the surrendering matrix [17–21]. Problematically, this circumstance leads to ambiguous local degradation phenomena including initiation, propagation [22–27] and noble-metal redistribution process (i.e. Cu) [28–30] over a nanoscopic length scale. A reliable approach of finding deterministic descriptors is to directly observe the nano-structural and compositional evolutions during local corrosion [31]. However, the challenges coming along with such research approaches have hampered experimental studies due to lack of experimental approaches that can probe the local degradation from early surface initiation to depth propagation in-situ and at a high spatial and temporal resolution. Therefore, the current understanding has been acquired through bridging and linking individual electrochemical and

* Corresponding author.
E-mail address: a.kosari@tudelft.nl (A. Kosari).

https://doi.org/10.1016/j.corsci.2020.108912
Received 25 June 2020; Received in revised form 24 July 2020; Accepted 29 July 2020
Available online 25 August 2020

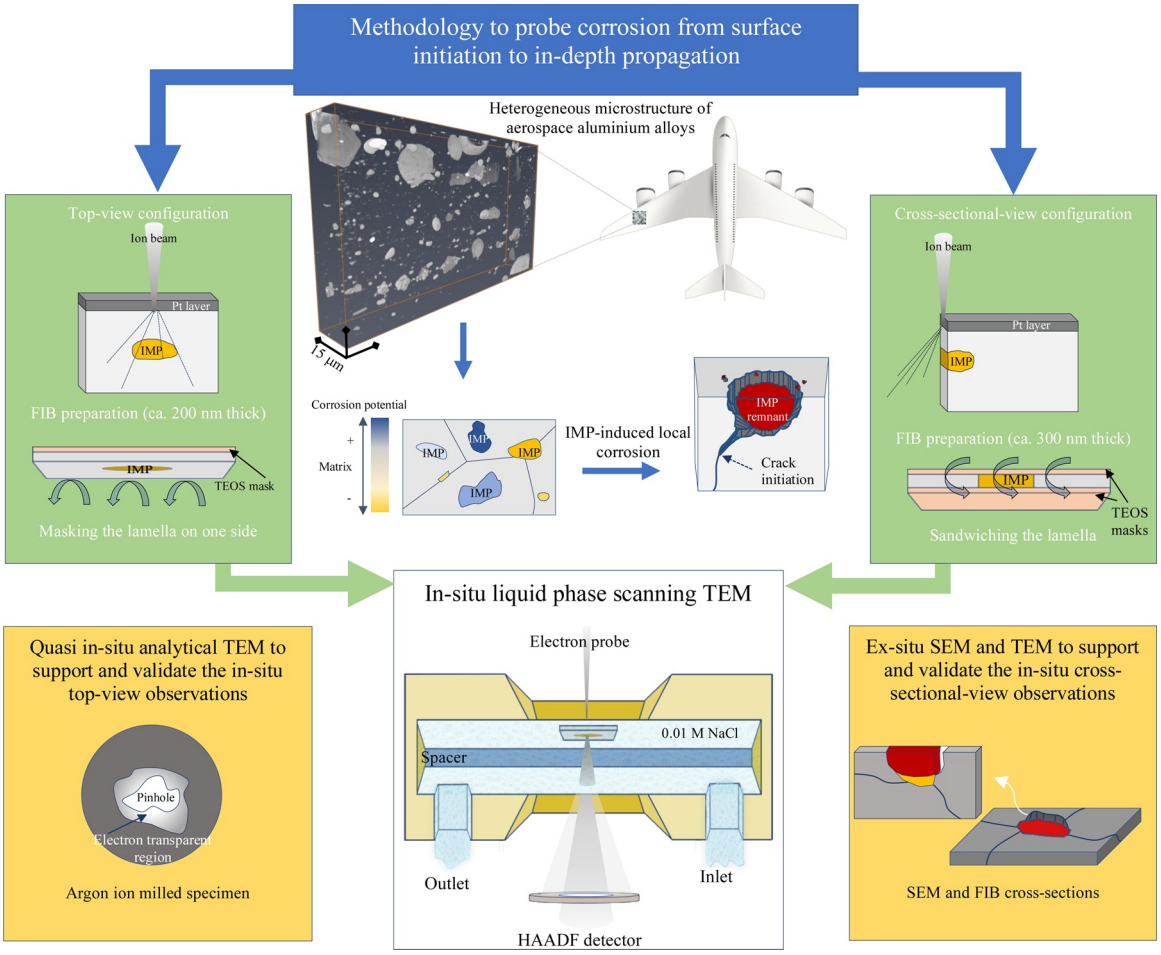

Fig. 1. Methodology for examining IMPs-induced corrosion degradation in aerospace aluminium alloys from surface initiation to in-depth propagation at the nanoscale. Three-dimensional reconstruction of aerospace AA2024-T3 microstructure (Movie S1) which leads to complicated corrosion. IMPs acquiring different corrosion potential and electrochemical activity in aqueous solutions are potential pit initiation sites. In-situ LP-TEM are performed in in HAADFSTEM mode on the treated lamellae of approx. 10µm´20 µm, representing 'real-life' corrosion. Top-view observations are provided by depositing a 25-nm-thick layer of tetraethyl orthosilicate (TEOS) using 2-keV electron-beam deposition; the corresponding schematic depicts the location of intermetallic particle (IMP) on the lamellae. For cross-sectional observations, the TEM specimen sandwiched between two 25-nm-thick layers of TEOS; note the location of intermetallic particle (IMP) on the lamellae. The prepared specimens are transferred to the home-made liquid cell using a FIB-based procedure, and each specimen is placed at the entrance side of the electron probe to mitigate the beam-broadening effect. Quasi in-situ analytical TEM experiments are conducted, in parallel, on argon ion-milled specimens (3-mm disk) to provide in-situ top-view observations with detailed structural and compositional information. Ex-situ examinations are carried out on FIB crosssections to support cross-sectional in-situ observations.

physicochemical studies [32–35] along with modelling and simulation studies [36–38], hence still explained in hypothetical terms.

Liquid phase TEM (LP-TEM) provides an unprecedented but challenging opportunity [39–44] to enhance the mechanistic understanding of interactions or dynamic in martials and particularly local corrosion at the nanoscale for complicated corroding systems [45,46]. However, it has contributed little to corrosion science up to now and it is mainly due to the lack of representing thin specimens of industrial alloys [47–50] and the subsequent challenging transfer to the delicate liquid cells [46,51,52]. Furthermore, the thin specimens can merely represent very early stages and this would be insufficiently informative for establishing comprehensive corrosion mechanisms. Here, we therefore treat specimens fabricated out of an industrial aerospace AA2024-T3 for a dedicated in-situ liquid phase transmission electron microscopy (LP-TEM), allowing for not only representative top-view (surface initiation) but also cross-sectional-view (depth propagation) observations of corrosion in-situ and at the nanoscopic level.

A schematic illustration of the methodology is shown in Fig. 1. As depicted, the oxidation direction is controlled by covering the specimens either on one side (in case of top view) or on both sides (cross-sectional view) by 25-nm-thick layers of tetraethyl orthosilicate (TEOS). The specimens that encompass precipitates of either Al_2CuMg (as a compound with a very complicated corrosion [53–56]) or Al_2Cu (a phase reported with a high cathodic electrochemical activity [21,57]) are fabricated with focused ion beam (FIB). The mask layer is electrochemically inert and promote no galvanic corrosion with the alloy specimen. The prepared specimens are transferred to the home-made liquid cell via a self-developed intricate procedure and each specimen is placed at the entrance side of the electron probe to mitigate the beam-broadening effect [58]. Top-view experiments show very early initiation events whilst the cross-sectional experiments provide insights into moderate stages of corrosion attack when the degradation propagates into the depth. In parallel, quasi in-situ and ex-situ TEM experiments are performed to obtain detailed chemical and structural analysis, and additionally to validate the in-situ results (Supplementary Materials). With that, we evidence that dynamics of local corrosion in AAs that are largely governed by dealloying attack to IMPs.

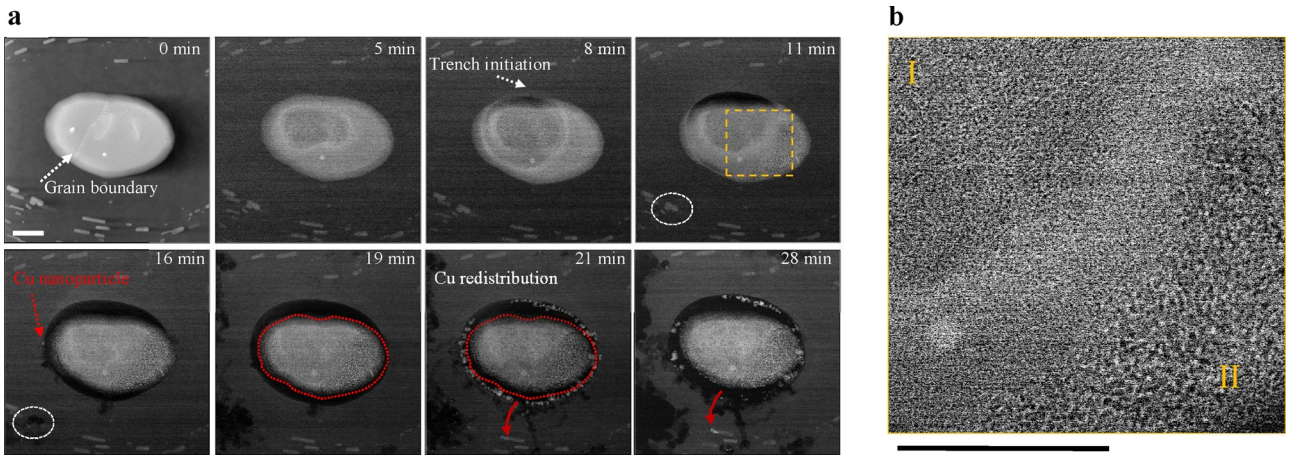

Fig. 2. In-situ top-view observations of local corrosion by S-phase (Al_2CuMg). (a) Time-resolved top-view HAADF-STEM images of an Al_2CuMg particle, showing morphological evolutions of the particle and its adjacent matrix (Movie S2; Probe current in vacuum 1.409 nA, Convergence angle 13.7 mrad, Camera length 185 mm, Magnification 20000X). The lamella is approximately 225 nm thick, in total. The electrolyte is 0.01 M NaCl (pH 6.5). The image taken at 0 min is in the absence of the electrolyte. The red dashed-lines border the particle area before and after the detachment from the alloy matrix. (b) Digitally-magnified view of the rectangular region shown in the STEM image taken at 11 min. The scale bar is 500 nm. (For interpretation of the references to colour in this figure legend, the reader is referred to the web version of this article).

2. Material and methods

2.1. In-situ liquid-phase scanning TEM (LP-TEM)

A Thermo-Fisher Helios G4 FIB/SEM armed with EasyLift NanoManipulator system was used to fabricate the TEM specimens (lamellae) out of regions of interest. To do so, high-current ion milling of a polished AA2024-T3 sheet was conducted until the appearance of an intermetallic particle within the milled region. To have the specimens more representative of bulk state microstructures, 200- to 300-nm-tick lamellae that were either masked on one-side or sandwiched by applying 25-nm-thick tetraethyl orthosilicate (TEOS) layers with 2-keV electron beam, giving either top- or cross-sectional-views to the electron beam. The deposition parameters are presented in Supplementary Materials. A novel sample transfer procedure was established to lift out and position the lamellae on the home-made chips without damaging the 25-nm thin SiN_x membrane (see Supplementary Materials). The chips were plasma cleaned for 1–1.5 min before assembling to get rid of contaminations and to make the surfaces hydrophilic, so that the electrolyte can easily run into the liquid cell. The electrolyte was 0.01 M NaCl open to 1 bar air pressure while the outlet was being sucked by a vacuum pump to have a very gentle flow during the experiments and also mitigate the bulging of the membranes [59]. The specimens were positioned at the entrance side of the electron probe to effectively mitigate the beam-broadening effect on the resolution in STEM mode. A home-made TEM holder that are specially designed for corrosion studies was used. A Cs corrected Thermo-Fisher Titan 300 kV TEM was employed to perform in-situ studies. High angle annular dark field (HAADF)-STEM imaging that has the advantage of showing Z-contrast and local thickness information was carried out at the probe current of 1.409 nA measured in vacuum. Snapshots of critical stages were taken at a fame time of 10 s^{-1} at various magnifications (either 20,000X or 28,500X) of 2048 × 2048 pixels using TEM Imaging and Analysis (TIA) software. Simultaneously, the movies were captured over the corrosion period with a fame time of 1 s^{-1} at various magnifications of 2048 × 2048 pixels using a screen recorder. The challenges in relation to the electron beam effect and sample artifacts on this part are discussed in Supplementary Materials.

2.2. Quasi in-situ analytical TEM

Quasi in-situ experiments were performed by repeatedly examining an identical location on argon ion-milled thin samples exposed intermittently to 0.01 M NaCl outside the microscope. After each cycle of exposure, the specimen was first rinsed off with distilled water for a few seconds and dried out carefully, followed by plasma-cleaning for 5 min before inserting to the TEM column. A Tecnai F20ST/STEM 200 kV was used for typical high resolution TEM imaging and scanning transmission electron microscopy/energy dispersive spectroscopy (STEM/EDS) elemental mapping and selected area electron diffraction (SAED) analysis. For EDS measurements, an Oxford Instruments X-MaxN 100TLE Windowless detector was used.

2.3. Ex-situ characterizations

AA2024-T3 sheets were hand-ground down to 1200 emery paper, followed by polishing using 0.5 and 0.05 μm alumina slurry in a non-aqueous solution on a soft cloth. Then the samples were exposed to 0.01 M NaCl for different exposure times. The surface morphology of the corroded samples was examined with secondary electron SEM. The thin cross-sections were fabricated out of corroded particles of interest with FIB and lift-out procedure, then examined with HRTEM, STEM-EDS and SAED methods.

3. Results and discussion

3.1. Local corrosion by S-phase (Al_2CuMg)

Time-resolved top-view morphological evolutions of S-phase as a result of interaction with 0.01 M NaCl are shown in Fig. 2a (Movie S2). High angle annular dark field-scanning TEM (HAADF-STEM), taken at 0 min in the absence of the electrolyte, shows a large bright particle of Al_2CuMg embedded in the alloy matrix. Note that HAADF-STEM images are highly sensitive to changes in spatial differences in atomic composition (Z-contrast). The Al_2CuMg particle consists of two grains and as indicated by the white arrow, a grain boundary can be distinguished inside the particle. After 5 min of exposure, the centre of the Al_2CuMg particle shows darker, implying less electron scattering due to material removal (corrosion). Note that the contrast becomes a bit poorer after introducing the electrolyte at t = 5 min due to scattering of electrons while traveling through the liquid. With prolonged exposure to the electrolyte (t = 8 min), the central corroded region radially grows in the same morphology which is ultra-finely porous. As indicated by the white arrow, a part of the adjacent matrix has partially dissolved

(trenching initiation), showing up dark in the HAADF-STEM image. At t = 11 min, the dissolution has extended more into the alloy matrix and the granular contrast variations are now visible over the whole corroding Al_2CuMg particle. The digitally-magnified view of the rectangular region shown in Fig. 2b reveals that the initially-corroded zone (Region I) is finely porous in morphology (pore size < 9 nm) whereas Region II has coarser porosities (15 nm < pore size < 20 nm). After 16 min, although no change in the particle morphology is seen (the grain boundary is not distinguishable any longer), the dark regions becomes evident further around the particle and into the alloy matrix, indicating a trench-shaped local dissolution. Furthermore, a bright spot that is circled in yellow appears at the edge of the matrix but it vanishes later (Movie S2). Besides, comparison of the circled-in-white region at 11 and 16 min reveals that a nanosized dispersoid ($Al_{20}Mn_3Cu_2$) has undergone corrosion and left a nano-pit behind. After 19 min, the matrix dissolution has entirely trenched all around the particle, indicating that the particle is electrically disconnected from the neighbouring matrix. At 21 min, numerous bright particles emerge all over the edge of the matrix and also on a dispersoid (mind the red arrow), shown later by diffraction analysis to be elemental copper nanoclusters. In addition, the Al_2CuMg particle size has considerably reduced between 19 and 21 min due to copper dissolution at this stage. With prolonged exposure (t = 28 min), we observe that some of the copper nanoclusters which are deposited around the trench rim disappear; we discuss this phenomenon later.

In-situ liquid phase HAADF-STEM clearly showed the evolution of a nanoporous morphology within S-phase caused by corrosion. In parallel, we have conducted complementary quasi in-situ TEM examinations on argon ion-milled disk specimens to acquire detailed compositional information at critical stages of corrosion. This also allows for assessing the potential effect of electron beam on the whole process, as discussed in Supplementary Materials. Fig. 3a shows HAADF-STEM imaging and energy-dispersive spectroscopy (EDS) mapping over the corroded parts of an Al_2CuMg particle after 10 min exposure to 0.01 M NaCl (see also Fig. S6). As can be seen, a nanoporous morphology has been established at some zones of the particle. Given the EDS results, we conclude that the selective dissolution of magnesium and to a lesser extent aluminium has occurred. The oxygen map is also a clear indication of corrosion taken place at morphologically-evolved zones; it also suggests the presence of aluminium hydroxide residing inside the pitted area.

To figure out what happens to copper at this very early stage of corrosion, further quasi in-situ investigations have been performed. Fig. 3b shows a STEM image of the pitted regions on an Al_2CuMg particle exposed to distilled water for 20 min (Fig. S5); this solution was chosen to slow down the corrosion process at very early stages. As is evident, the pits and the intact region are boarded by the bright narrow rims which are actually surface-diffused copper (see Fig. S5). Note that the pits appear darker in the HAADF-STEM image due to local mass loss by selective dissolution. Thus, dealloying attack is clearly responsible for corrosion initiation on S-phase. In fact, dealloying selectively depletes active elemental components of the phase (herein aluminium and magnesium) to evolve a nanoporous Cu morphology.

Fig. 3c shows a HAADF-STEM image of an Al_2CuMg particle intermittently exposed to 0.01 M NaCl for a total exposure of 30 min. The EDS analysis reveals that the particle is depleted from magnesium and aluminium (see Fig. S6); it is almost empty of magnesium (0.2 at%) and contains approx. 6.3 at% after 30 min. Note that the particle is still connected to the alloy matrix and the copper redistribution process has not occurred. As can be seen, the copper dendrites are formed at the trench region (Fig. $3c_1$). Further analysis including EDS mapping and HRTEM imaging identify them as nanoclusters of Cu_2O (Fig. $3c_2$). This form of copper is sourced from solid solution, which holds 0.2 − 0.5 at% copper, as a consequence of the simultaneous matrix dissolution and surface diffusion [11]. In fact, the copper in the matrix solid solution gradually accumulates during the trenching to form copper nanoclusters. However, they later become electrically isolated in the aluminium oxide products and undergo oxidation themselves. Looking at the oxygen map corresponding to the rectangular region, we see some local corrosion spots on the alloy matrix. As shown in Fig. $3c_3$, these are nano-pits that are formed due to the passive layer breakdown. The corresponding EDS map reveals the surface-diffused solid-solution copper as a rim around the pit where the alloy matrix is locally dissolved.

Cross-sectional-view HAADF-STEM sequences of a sandwiched S-phase being exposed in-situ to 0.01 M NaCl solution are shown in Fig. 4a (Movie S3). The image taken in the absence of the electrolyte (t = 0 min) shows an Al_2CuMg particle which is confined in the alloy matrix. The snapshot taken after 15 min reveals some contrast variations on the upper part of the particle which is bare and interacting with the electrolyte. As can be seen, corrosion has slightly dissolved the surrounding alloy matrix while it has propagated more into the particle than the matrix, resulting in a nanoporous morphology. After 20 min, the corrosion process changes in morphology. It penetrates deeper at the particle/matrix interface associated with the extensive matrix dissolution. The snapshot taken at 25 min shows the deep corrosion propagation equally into the matrix and the interfacial regions of the particle but shallower into the middle part of the particle. The trench grows in width and depth during the corrosion process until it is about to undercut the particle after 28 min; the middle part of the particle is not fully corroded at this point. Fig. 4b compares the digitally-magnified view of the rectangular region at 15 and 28 min, revealing formation of the nanoparticles at the top of the corroding particle which have considerably grown in size and number since the beginning of the exposure. The snapshot taken at 31 min shows that the particle disconnected from the alloy matrix. Like the top-view findings, the latest-corroded region shows up in a course nanoporous morphology. Due to rapid dealloying at this stage (Movie S3), a breakdown crack takes place near the top of the particle, indicated by the yellow arrow. At t = 34 min, numerous nanoparticles are formed at the edge of the matrix whereas the particle has decreased in size and also the bright layer atop the corroding particle has disappeared. Fig. 4c shows the involvement of a deep intermetallic particle in corrosion propagation at an advanced stage. As is evident, the corrosion has penetrated quite deep induced by the redistributed copper nanoclusters until reaching another Al_2CuMg particle underneath. This can well explain how corrosion further propagates into the depth with prolonged exposure time. In addition, comparison of the particle size before corrosion (t = 0 min) and after 37 min reveals a considerable shrinkage due to selective aluminium and magnesium dissolution and following copper liberation.

Fig. 5a and b show top-view SEM, cross-sectional STEM/EDS and selected areas electron diffraction (SAED) patterns on the bulk-corroded samples exposed ex-situ to 0.01 M NaCl for 15 min and 6 h, respectively. The SEM image in Fig. 5a depicts a narrow trench around the particle which has a smooth surface due to a fine corrosion-attack morphology. The cross-sectional HAADF-STEM image of the corresponding particle shows that it is corroded partly and corrosion has penetrated deeper at the particle/matrix interface (in agreement with the in-situ observations). The EDS analysis shows that the corroded region which is uniformly nanoporous in morphology has almost been depleted in magnesium (1.3 at%) but still contains 11 at% aluminium, indicating the occurrence of dealloying. In addition, a narrow layer of nanoclusters on the top of the particle (Region II) is clearly distinguishable from the rest (Region I). Using SAED analysis, we characterized Region II as elemental copper nanoparticles whereas Cu and Cu_2O coexist in Region I. Comparatively, the surface of the particle exposed for 6 h is quite rough, associated with numerous deposited nanoclusters around and in the trench (Fig. 5b). The cross-sectional STEM image shows that the particle is fully corroded and disconnected from the matrix. Variations in pores size are observed all over the remnant, probably referring to different stages of corrosion within the particle. In addition, there are the signs of breakdown on the top of the

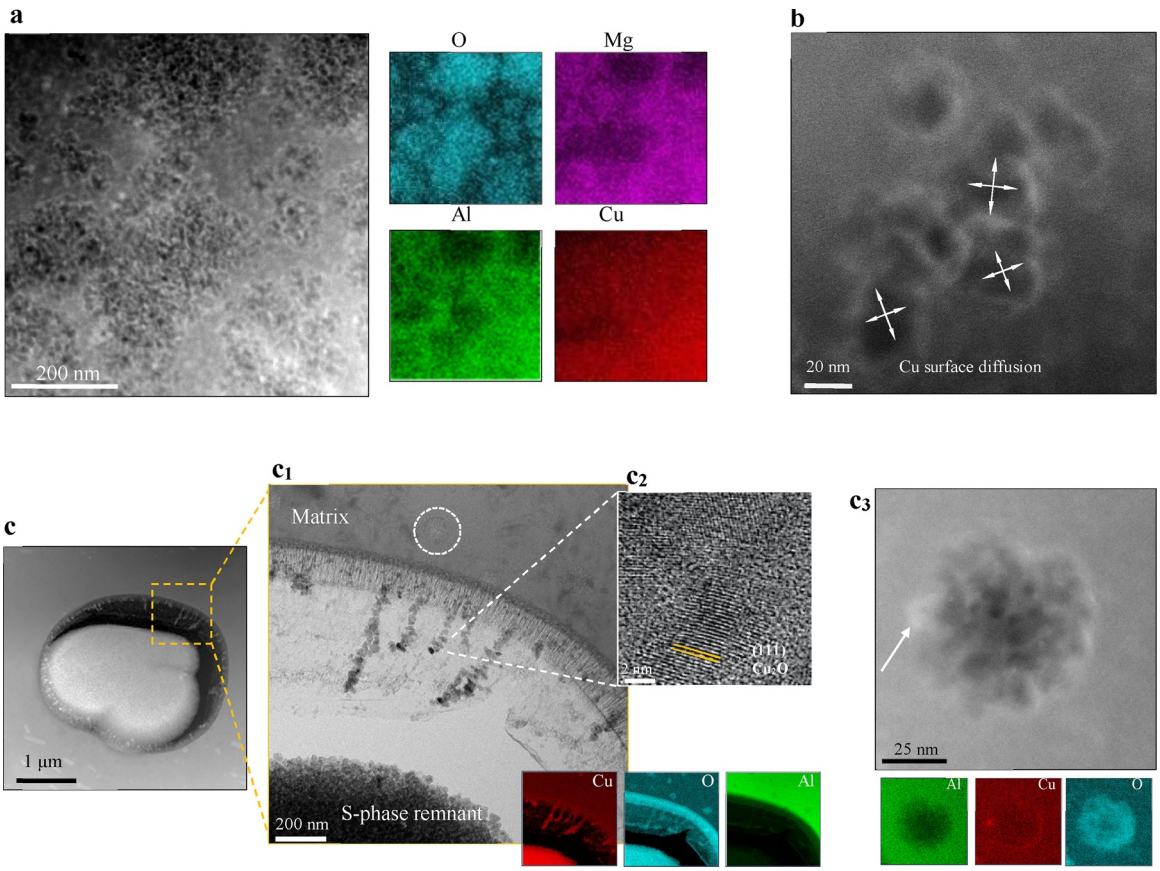

Fig. 3. Analysis of corroded S-phase intermediately exposed to 0.01 M NaCl. (a) STEM/EDS analysis of an Al_2CuMg particle exposed to 0.01 M NaCl for 10 min; the elemental map reveals selective dissolution of aluminium and magnesium to different extents (Fig. S6). (b) HAADF-STEM image of an Al_2CuMg particle exposed to distilled water for 20 min, revealing the single pits and copper surface diffusion (Fig. S5). (c) HAADF-STEM image of an Al_2CuMg particle taken after 30 min of exposure to 0.01 M NaCl (Fig. S6). (c1) TEM image and corresponding EDS map are related to the dashed rectangular region shown in the STEM image. (c2) High resolution TEM (HRTEM) image of the region indicated by the white dashed lines. (c3) STEM/EDS analysis of a single pit on the alloy matrix where the region is circled in the TEM image, revealing redistribution of solid-solution Cu as a rim around the pit. Notice that the results are obtained via quasi in-situ TEM experiments on thin argon ion-milled specimens (Fig. S5 and Fig. S6).

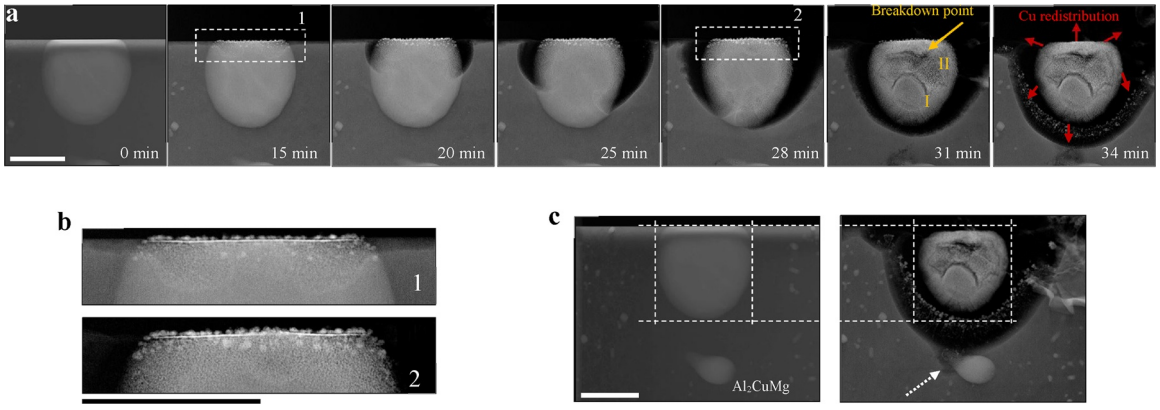

Fig. 4. In-situ cross-sectional observations of local corrosion by S-phase (Al_2CuMg). (a) HAADF-STEM time series of cross-sectional dealloying-driven evolutions in a sandwiched Al_2CuMg particle (Movie S3; Probe current in vacuum 1.409 nA, Convergence angle 13.7 mrad, Camera length 185 mm, Magnification 28500X). The yellow arrow indicates the breakdown location. The red arrows indicate the copper dissolution from the top and the periphery of the corroded particle. (b) Digitally-magnified view of the rectangular region shown in the STEM images taken at 15 min (No.1) and 28 min (No. 2). (c) Comparison of the particle size before and after 37 min of exposure. The white arrow indicates the involvement of a deep Al_2CuMg in corrosion propagation at an advanced stage. The specimen thickness is 350 nm including the TEOS layers. The electrolyte is 0.01 M NaCl (pH 6.5). (For interpretation of the references to colour in this figure legend, the reader is referred to the web version of this article).

particle (indicated by the yellow arrow) where the layer of copper nanoparticles is missing. We identified the undercut particle as a Cu_2O nanoporous remnant which is covered by $Al(OH)_3$. The SAED pattern collected from the cluster (circled in red) shows spots matching elemental copper. With this compositional insight, we draw your attention back to Fig. 4a where the copper nanoclusters on the top of the particle, increasing in size and number, dissolve away after the particle undercut event (t = 29 min).

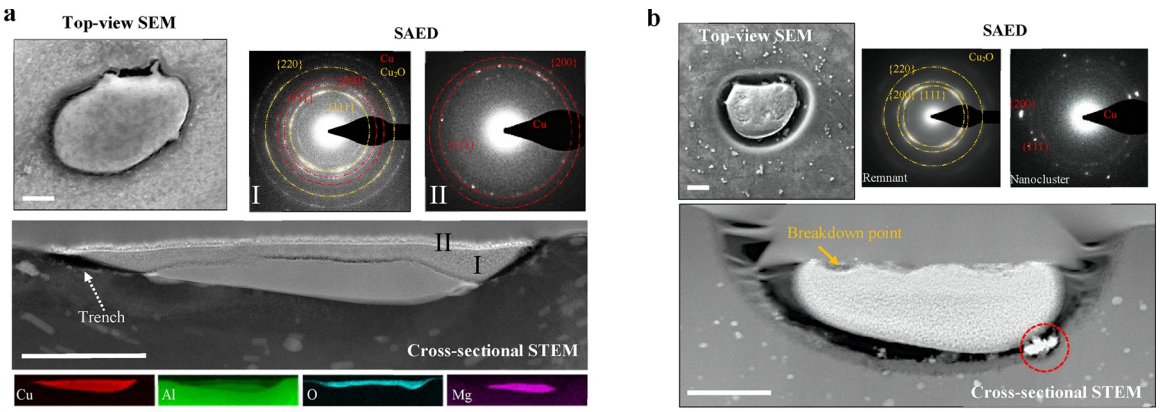

Fig. 5. Post-mortem analysis of corroded Al_2CuMg particles exposed to 0.01 M NaCl. (a) Top-view SEM, cross-sectional STEM/EDS and SAED analysis of an Al_2CuMg particle immersed in 0.01 M NaCl for 15 min. The SEAD patterns show characteristic rings and spots for Cu and Cu_2O; the close lattice parameters are not indexed. (b) Top-view SEM, cross-sectional STEM and SAED analysis of an Al_2CuMg particle immersed in 0.01 M NaCl for 6 h. Note that the matrix and the particle are not at the same level where the nanoclusters nestled in the trench are identified as elemental copper. This undercut particle is a nano-porous Cu_2O remnant covered by $Al(OH)_3$. The cross-sections are fabricated out of the corresponding corroded particles with FIB. The scale bar is 1 μm.

3.2. Local corrosion by Al_2Cu (θ-phase)

Fig. 6a shows top-view sequences of an Al_2Cu particle in 0.01 M NaCl. The HAADF-STEM image is taken at 0 min in the absence of the electrolyte. After 37 min, a few nanoparticles (bright spots) appear at the edge and on the top of the corroding particle; there is no sign of matrix corrosion (trenching) up to this point. We observe that the nanoparticles are growing in size, and this is associated with a slight corrosion attack to the particle, itself, in particular to the edge region (t = 57 min). A comparison of the electron intensity along the dashed

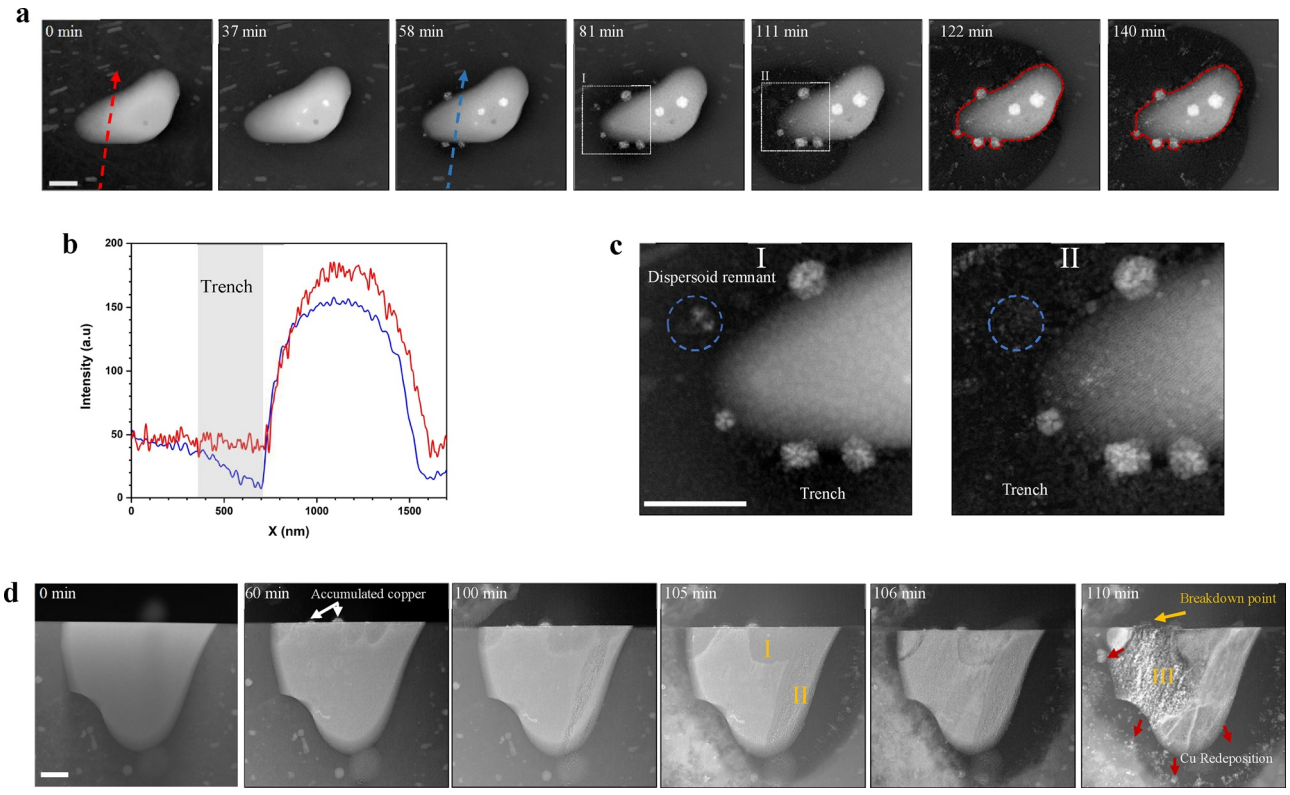

Fig. 6. In-situ top-view and cross-sectional-view observations of local corrosion by θ-phase (Al_2Cu). (a) HAADF-STEM time series of top-view dealloying-driven evolutions within an Al_2Cu particle and its adjacent alloy matrix (Movie S4; it is made of 52 snapshots taken at different stages of an exposure for 149 min at the camera length of 75 mm). The red dashedlines indicate the particle area before and after the detachment. The lamella is approximately 200 nm thick, masked with 25-nm-thick TEOS layer on one side. (b) Electron intensity along the red and blue arrows in Fig. 6a, proving the trenching occurrence which follows the dealloying attack to the particle. (c) Digitally-magnified HAADF-STEM images of Region I and II in Fig. 6a, showing the transition from the globular to river-like dealloying morphology. The circled-in-blue region shows a dispersoid particle undergoing dealloying and then disappearing. (d) Cross-sectional dealloying-driven evolutions in a sandwiched Al_2Cu particle, captured by HAADF-STEM (Movie S5; Probe current in vacuum 1.409 nA, Convergence angle 13.7 mrad, Camera length 75 mm, Magnification 20000X). The total specimen thickness including TEOS layers is 350 nm. The white arrows point to the surface-diffused accumulation of copper. The yellow arrow points the breakdown location on the top of the particle. The red arrows indicate the copper dissolution merely from the periphery of the dealloyed particle at the trench bottom. The electrolyte is 0.01 M NaCl, pH 6.5. The scale bar is 500 nm. (For interpretation of the references to colour in this figure legend, the reader is referred to the web version of this article).

lines (the blue and red line) clearly discloses the matrix trenching and also the corrosion attack to the particle (Fig. 6b). At this stage, additional information via quasi in-situ STEM/EDS confirms selective aluminium dissolution from the particle itself (θ-phase dealloying), resulting in the trenching of the closest matrix to the dealloyed region (Fig. S7 and S9). As corrosion progresses until 81 min, a globular corrosion morphology (~20 nm scale) becomes more apparent on the particle, however, it turns into a banding morphology (~10 nm spacing) after 111 min. The transition from the globular to the band-like morphology can be seen in the digitally-magnified views in Fig. 6c. After 111 min, the alloy matrix has significantly been dissolved which is also associated with corrosion of nanosized dispersoids ($Al_{20}Mn_3Cu_2$), leaving several bright spots behind (Fig. 6c). This behaviour continues until the whole particle is about to get disconnected (t = 122 min); numerous nanoparticles are accumulated on the particle at this stage. During the next 18 min, the corrosion proceeds further with the matrix trenching and slight particle corrosion. Besides, we observe no considerable change in the particle size where fewer nanoparticles are formed at the edge of the trenched matrix (Movie S4), compared to S-phase.

Fig. 6d shows cross-sectional in-situ observations of θ-phase-induced local corrosion, taking place to the sandwiched specimen. Comparing the HAADF-STEM image taken at t = 0 min and 60 min reveals the corrosion initiation at several locations in the Al_2Cu particle itself; the dark region within the particle shows a fine nanoporous morphology. The snapshot taken after 60 min reveals how corrosion has propagated into the depth; the white arrows point to two bright nanoparticles accumulated on top of the particle. In spite of a higher corrosion potential of θ-phase than the alloy matrix, it seems that its self-corrosion precedes the dissolution of the matrix (trenching) which is covered by an isolating passive layer. After 100 min, corrosion has penetrated deeper, probably due to structural defect variations at the right side of the particle while the alloy matrix is slightly dissolved on the top. Looking at the STEM images of the particle taken after 105 min, we see that the initially-corroded region within the particle has a finer nanoporous morphology (Region I) than the later-corroded part (Region II) where the matrix is significantly corroded. From this point, it takes about 1 min for the particle to be undercut and extensively corroded (t = 106 min). Note that similar to S-phase, the latest-corroded part of the particle is coarsest in morphology (Region III). At 110 min, we see the breakdown event right on top of the particle; associated with the appearance of redeposited nanoparticles, in particular, at the bottom of the trench (Movie S5) which is less in number as compared to S-phase.

Post-mortem analysis of the samples related to θ-phase-induced local corrosion are shown in Fig. 7. Cross-sectional STEM image of an Al_2Cu particle exposed for 15 min (Fig. 7a) reveals formation of the nanoporous layer all over the top of the particle; the depth penetration of the layer is location-dependent. A closer look at this particle is shown in the inset; additional STEM/EDS reveals the selective dissolution of aluminium (dealloying) associated with accumulation of copper nanoparticles at the particle/matrix interface. Fig. 7b shows a high resolution TEM image taken from the nanoporous region of a dealloyed Al_2Cu particle (Fig. S9a), revealing co-existing nano-sized Cu and Cu_2O nanoparticles. Further investigations are carried out on a representative Al_2Cu particle corroded for 6 h, as shown in Fig. 7c. The top-view SEM image reveals a trench around the particle which has a wide opening tapered down into the depth. In addition to the layer of copper nanoparticles on the top, the cross-section shows a gradient nano-porous morphology where pore size increases towards the depth. The composition line scan reconstructed from the rectangular region in the STEM image clearly reveals selective dissolution of aluminium: its amount slightly rises with the distance from the top. This phenomenon is consistent with diffusion of selectively dissolved aluminium to the top before leaving the particle. Fig. 7d shows an Al_2Cu particle exposed for 19 h. The SEM image reveals that the particle surface and its adjacent matrix are corroded severely. The further analysis on the corresponding lifted-out cross-section confirms formation of an undercut Cu_2O remnant covered with aluminium hydroxide where a few copper nanoclusters are nestled in the trench; additional evidence can be found in Fig. S9.

3.3. The role of copper-rich regions in local corrosion

Up to this point, both in-situ liquid phase and analytical post-mortem TEM examinations unanimously narrate that the IMPs-induced local corrosion initiation is a consequence of a preceding dealloying attack occurring to both S-phase and the θ-phase compounds. This form of corrosion results in the formation of copper-rich regions within IMPs that are electrochemically nobler than the un-corroded regions and the adjacent alloy matrix, leading to nano-galvanic interactions between these nanoscale heterogeneities. Here, we prove that the nanoscopic copper-rich region can function as strong cathodic sites, supporting ORR reactions that leads to highly local alkaline solution chemistry. Besides, as long as the alloy matrix is covered by the aluminium oxide passive layer which is isolating in nature, it would be protected and cannot support any electrochemical reactions. However, if the alloy matrix undergoes local breakdown due to chloride attack, solid-solution copper does also surface diffusion to around nanoscopic corrosion pits, hence acting as nano-cathodic sites as well. This has been fulfilled by analysis of the S-phase/θ-phase composite particles [60] exposed to a solution of 0.003 M $Ce(NO_3)_3$ + 0.01 M NaCl. According to E-pH diagram of cerium [61], $Ce(OH)_3$ can precipitate in solution pH approximately above 10 via a chemical reaction, it can therefore be a pH marker.

Fig. 8a shows STEM/EDS analysis of an Al_2CuMg/Al_2Cu composite particle exposed to 0.003 M $Ce(NO_3)_3$ + 0.01 M NaCl for 70 min. As can be seen, cerium has deposited discretely around the rims of the pits formed on the Al_2CuMg particle, neither on θ-phase nor the alloy matrix. In fact, an alkaline environment is required for triggering Ce deposition, this phenomenon proposes a nano galvanic coupling establishment between Cu-rich regions on the Al_2CuMg particle (cathodic sites) and inside the pits (anodic sites). Since cathodic reactions produce OH^-, we can claim that the surface-diffused copper on the corroded region of S-phase support the cathodic reaction like oxygen reduction reaction (ORR), leading to cerium deposition. Further evidence is shown in Fig. 8b, where the cross-sectional STEM/EDS analysis of an Al_2CuMg/Al_2Cu composite particle clearly reveals the precipitation of cerium hydroxide over the Al_2CuMg particle. The results herein prove that dissimilar intermetallic particles do not establish cooperative corrosion at least at early stages of corrosion owing to their different electrochemical behaviour. There is no nobility inversion and IMPs are in fact simultaneous anodic and cathodic sites since the beginning of exposure that can also form nanogalvanic coupling with the closest corroding alloy matrix.

Furthermore, Fig. 9 shows how a copper nanocluster can drive the matrix corrosion through a consecutive deposition/dissolution process. As can be seen, the cluster establishes nano-galvanic coupling with the adjacent matrix, leading to the local matrix corrosion. This phenomenon can gradually trench around the cluster until the electrical disconnection occurs. Then, the nanocluster can acquire its free corrosion potential at which copper dissolves. Upon the release of copper into the electrolyte, it reappears as smaller nanoparticles at the edge of the matrix where thermodynamically copper redeposition is favoured, followed by further corrosion of the alloy matrix (Movie S6).

4. Dealloying-driven local corrosion mechanism by Al_2CuMg and Al_2Cu

Here, in-situ direct nanoscopic top-/cross-sectional-view observations along with detailed supplementary information allow us to provide a comprehensive mechanism explaining local degradation

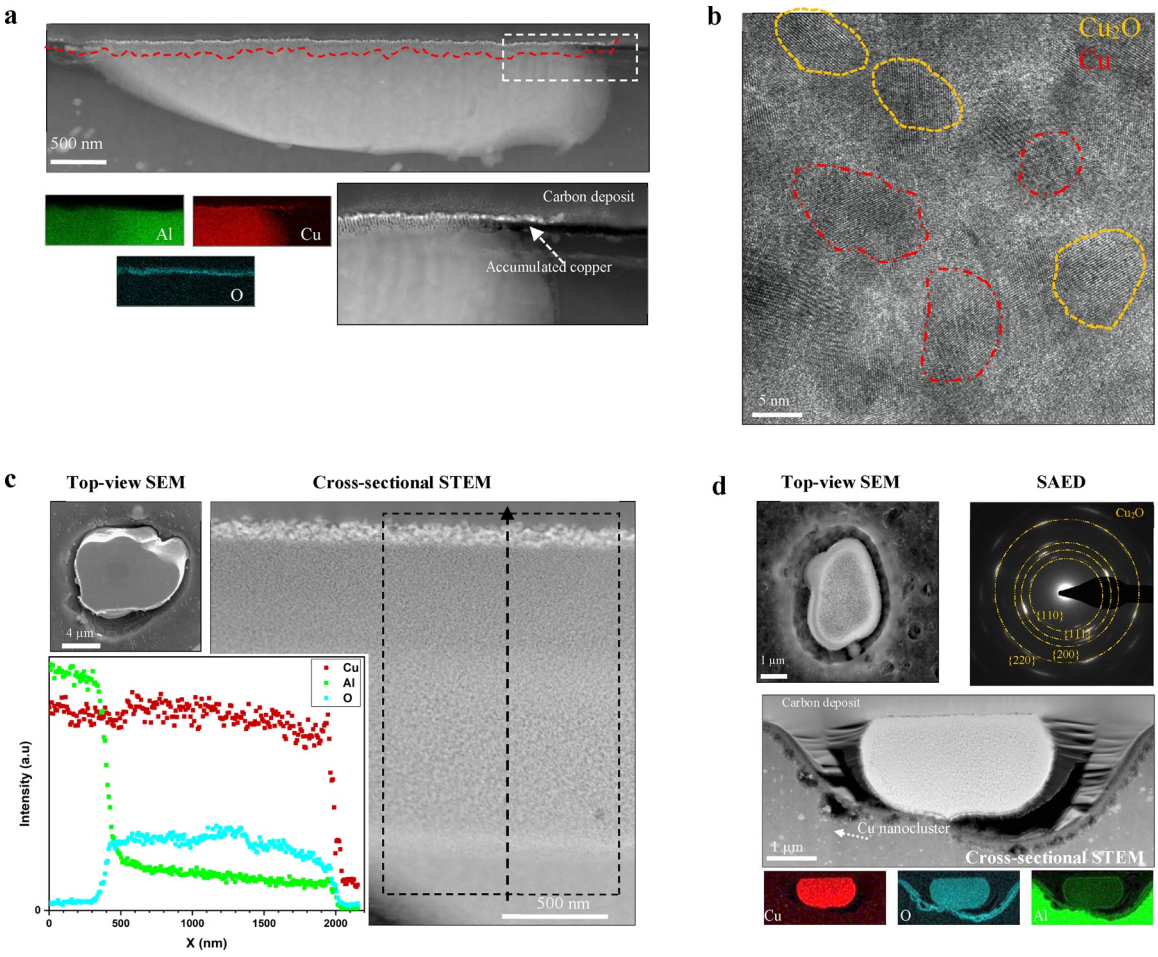

Fig. 7. Analysis of post-corroded Al_2Cu particles (θ-phase). (a) Cross-sectional HAADF-STEM image of an Al_2Cu particle exposed to 0.01 M NaCl for 15 min, showing several locations attacked by dealloying. The inset is the magnified view of the rectangular region analysed by STEM/EDS; the white arrow points the accumulated copper at the edge. (b) HRTEM image taken from the dealloyed region of an Al_2Cu particle corroded for 15 min, revealing coexisting Cu and Cu_2O nanoparticles (identified from the lattice plane spacings). (c) Top-view SEM, cross-sectional STEM/EDS analysis of an Al_2Cu particle immersed in 0.01 M NaCl for 6 h. The SEM image shows the smooth surface of the particle surrounded by a trench with a wide opening. The graph is the elemental profile reconstructed from the rectangular region in the cross-sectional STEM image, showing selective dissolution of aluminium. (d) Top-view SEM, cross-sectional STEM/EDS and SAED analysis of an Al_2Cu particle immersed in 0.01 M NaCl for 19 h. The remnant is characterized as a nano-porous Cu_2O particle covered by aluminium hydroxides.

phenomena related to precipitates hardening phases of Al_2CuMg and Al_2Cu and also controversial Cu redistribution. Local corrosion is here divided into three distinct stages including surface initiation, in-depth propagation, and particle undercut and Cu release. Fig. 10 schematically depicts different stages of local corrosion induced by S-phase and θ-phase in AAs where the probable electrochemical reactions occurring around the IMPs are shown in detail. It also shows the local solution chemistry and compositions at different locations of S-phase and θ-phase (this form of representation of the pores is inspired by Snyder et al. [12]).

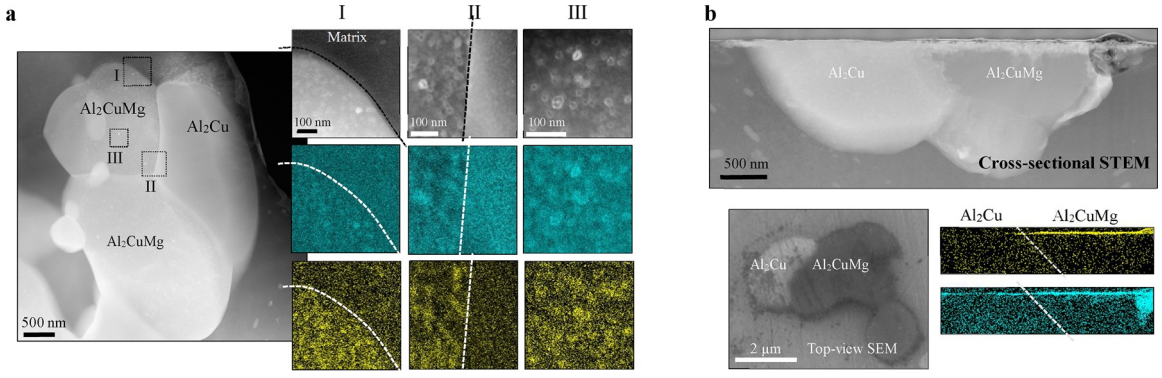

Fig. 8. Analysis of S-phase/θ-phase composite particles in 0.003 M $Ce(NO_3)_3$ + 0.01 M NaCl. (a) HAADF-STEM/EDS analysis of an Al_2CuMg/Al_2Cu composite particle on an argon ion-milled disk at different regions. The disk is exposed to 0.01 M NaCl + 0.003 $Ce(NO_3)_3$ for 70 min (blue: O and Yellow: Ce). (b) Cross sectional STEM/EDS images of an Al_2CuMg/Al_2Cu particle exposed to 0.01 M NaCl + 0.003 $Ce(NO_3)_3$ for 90 min; revealing a thin layer of cerium oxide deposited on the Al_2CuMg not on the Al_2Cu. The inset is top-view SEM image of the mixed particle before milling (blue: O and Yellow: Ce).

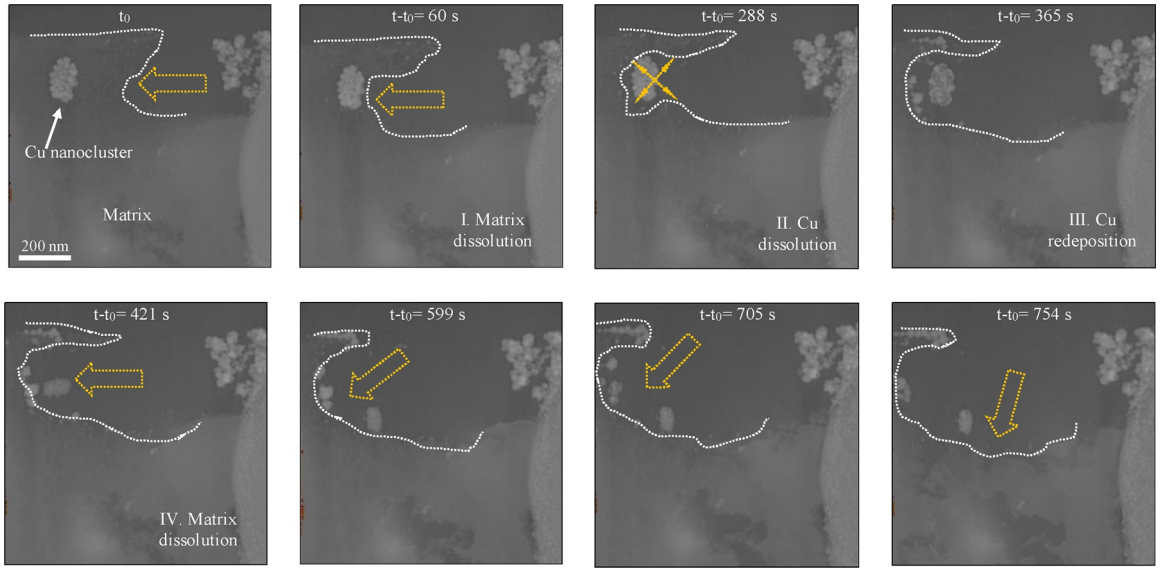

Fig. 9. The role of copper nanoclusters in corrosion propagation. Time-resolved HAADF-STEM images, showing how a copper nanocluster leads to local dissolution of the matrix. (Movie S6; Probe current in vacuum 1.409 nA, Convergence angle 13.7 mrad, Camera length 185 mm, Magnification 28500X). The sample is approx. 200 nm thick and is sandwiched between two layers of TEOS.

4.1. Surface initiation

Local corrosion initiates by dealloying attack to IMPs but stabilizes (continuous corrosion) through nanogalvanic interactions between copper-rich regions and the IMPs. This condition gradually gives rise to a local solution chemistry in which the passive layer covering the nearby alloy matrix cannot survive, leading to its local dissolution. For S-phase, the surface initiation process happens rather shortly after exposure as magnesium is highly soluble in the studied solution, although hydrolysis of aluminium ions occurs simultaneously and can passivate some active locations. Copper does surface diffusion and appears in rims around the pits (Fig. 3b), subsequently rearranging in a nanoporous morphology (Fig. 3a). Although, copper cannot thermodynamically dissolve at this stage, it can be released via dissolution of physically-detached Cu clusters. In the case of θ-phase, $Al(OH)_3$ formation inhibits corrosion at initial dissolution sites and consequently a sluggish initiation process provides copper with sufficient time to accumulate as nanoparticles on the surface in particular at the edges (Fig. 6a). Afterward on both S-phase and θ-phase, nanogalvanic interactions are established between anodic zones and the copper-rich cathodic sites supporting OH^--producing reactions. Since $Al(OH)_3$ is merely stable at pH 4–9, the aluminium oxide passive layer of the nearest alloy matrix destabilizes due to local chemistry provoked by electrochemical reactions, resulting in the trench initiation (Fig. 2a and Fig. 6a).

4.2. In-depth propagation

During the depth propagation, cathodic reactions like oxygen reduction reactions (ORR) take place on the upper parts of the corroding IMPs while the intact part of the particle and the adjacent matrix undergo anodic dissolution. For S-phase, owing to a rapid dealloying propagation and trenching (anodic process), the rate of cathodic reactions is also rather high (to maintain overall charge neutrality), resulting in an extremely basic local chemistry atop a corroding S-phase. On the other hand, the massive exit of the corrosion products due to fast dealloying leads to the detachment of some copper-rich segments from the upper part which is highly porous (Fig. S8a). Then, the detached copper segments obtain their free-corrosion potential and endure anodic dissolution. However, the consequent copper ions become redeposited either mostly onto the same corroding particle (Fig. 4a) since the top part shows cathodic activity or on the Cu-rich regions on the alloy matrix undergoing active local dissolution (Fig. 2a at 16 min). Under hydrodynamic conditions, the copper ions can be carried away by the flowing electrolyte and re-plate on distant active sites like the local cathodes on the matrix. The depth propagation happens significantly slower to θ-phase and consequently a moderate basic local chemistry is built up atop a corroding particle. That explains findings of other researches in which S-phase, in cerium-inhibited solutions, is found with a thick layer of the cerium hydroxide [62] triggered by local alkalinity while θ-phase is only slightly/partly covered [63]. Additionally, due to hydrolysis of metal ions, the pore and trench environments would experience a pH gradient with lower acidity towards the top of IMPs [12]. In the region with moderate pH, aluminium hydroxide gel is stable and physically covers of the sections involved in dealloying. This mechanism is valid for both S-phase and θ-phase, but takes longer for the latter. On the other hand, the sluggish evolutions give produced H^+ ions more time to diffuse away; thus, the trench and pore environment within the corroding Al_2Cu particles are less acidic as compared to those for the S-phase. During the progress of dealloying, the corroding IMPs enrich in copper and acquire higher corrosion potential, leading to formation of a coarser nanoporous morphology than the earlier-dealloyed regions. Note that the corrosion potential of the whole specimen is insufficiently high for direct copper corrosion before the particle undercut; however, Cu_2O nanoparticles can form as a result of physical or electrical isolation of some copper segments, enduring oxidation during the dealloying course (Figs. 4a, 5 a and 7 b).

4.3. Particle undercut and Cu release

As soon as the trenching undercuts the whole corroding particle, its corrosion potential rapidly goes up whereby direct dissolution of copper can occur. This event is also associated with a breakdown in the corroding IMPs due to massive dissolution and egress of the corrosion products. At this stage, the difference in behaviour of S-phase and θ-phase is the amount of copper ions they can release into the solution. Since a corroding θ-phase particle is largely covered with aluminium hydroxide gel, it gradually transforms into a Cu_2O remnant after the undercut; mostly the bottom part of θ-phase particles contributes to copper release. In contrast, S-phase contributes to redistribution of copper to the largest extent as the upper part and the periphery of the undercut particles liberate copper, followed by re-plating at aluminium

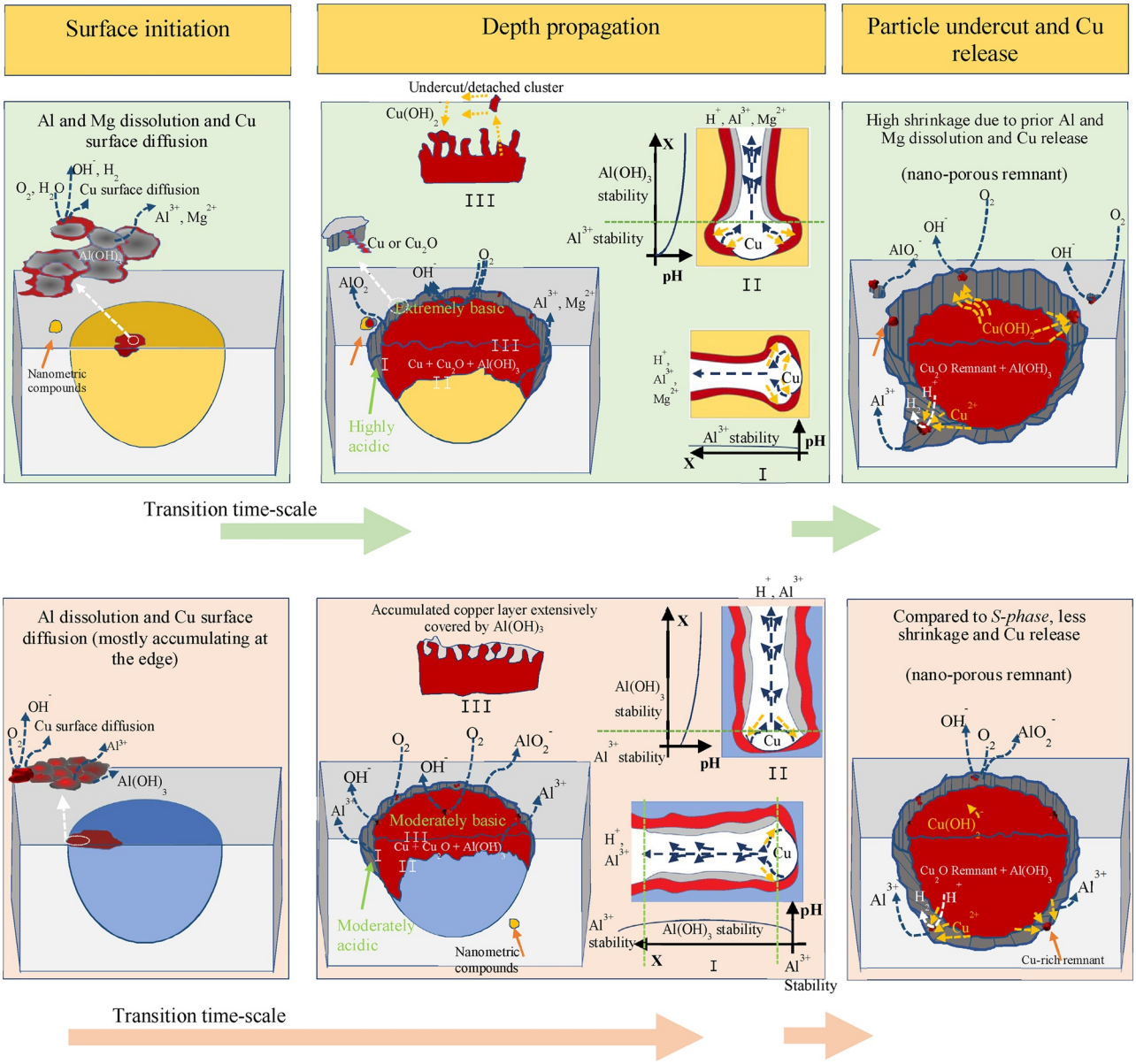

Fig. 10. Dealloying-induced IMPs-induced local corrosion mechanism. 3D schematic view of localized corrosion initiation induced by individual S-phase (boxed in green; upper row) and θ-phase (boxed in pink; lower row) particles embedded in the alloy matrix. The mechanism by which the corrosion initiates at the surface and propagates into the depth is shown. The probable corrosion reactions occurring around IMPs are depicted in detail. In addition, local solution chemistry and compositions at different locations on S-phase and θ-phase are shown. (For interpretation of the references to colour in this figure legend, the reader is referred to the web version of this article).

hydroxide-free parts of the matrix surface. As other sources of redistributed copper, corroded nanometric copper-containing particles like dispersoids (Fig. 6c) and also the alloy matrix which holds approx. 0.5 wt.% Cu in solid solution (Fig. 3a) can be enumerated. Furthermore, the deposited copper nanoclusters can establish local nanogalvanic coupling with the matrix and promote further local corrosion. As evidenced (see Fig. 9), they show an iterative process of redeposition/dissolution through which coppers nanocluster speed up the aluminium dissolution until they get detached from the matrix. Then, the free-standing particles undergo anodic dissolution themselves, followed by redepositing back on the matrix and continue to further corrode the alloy matrix. Note that the local corrosion from the initiation to particle undercut occur to S-phase in a shorter time-scale, thus early copper ions liberated from the undercut S-phase can also be redeposited on the neighbouring θ-phase and other active intermetallic compounds.

5. Conclusion

In-situ top- and cross-sectional-view liquid phase STEM directly evidenced different stages of corrosion from surface initiation to in-depth propagation where different time-scales were observed for S-phase and θ-phase. We stress the pivotal role of dealloying attack to IMPs as the precursor of local degradations in AAs. IMPs are in fact simultaneous anodic and cathodic sites as from the beginning of exposure. Nanogalvanic interactions between the heterogeneities within the corroding IMPs themselves, and later with the closest neighbouring alloy matrix stabilize the local corrosion. S-phase is more problematic in terms of corrosion as it induces local degradation in a relatively short exposure time and largely contributes to copper redistribution, compared to that for θ-phase. The current findings can fully explain controversial forms of IMPs-induced local corrosion in AAs like pitting and intergranular corrosion, and the copper redistribution process. Besides,

they constitute a basis for reliable predictive corrosion modelling and simulation and can be used to develop smart corrosion inhibition strategies for AAs. Furthermore, the experimental package can be applied to studies in relation with corrosion of other complicated systems like stainless steels and also fabrication of advanced nanoporous materials like sensors and catalysts.

Data and materials availability

All the data needed to assess the conclusions in the work is presented in the paper and/or the Supplementary Materials.

CRediT authorship contribution statement

A. Kosari: Conceptualization, Methodology, Validation, Investigation, Writing - original draft. **H. Zandbergen:** Conceptualization, Resources, Writing - review & editing, Supervision. **F. Tichelaar:** Conceptualization, Investigation, Writing - review & editing. **P. Visser:** Conceptualization, Writing - review & editing. **P. Taheri:** Conceptualization, Writing - review & editing. **H. Terryn:** Conceptualization, Writing - review & editing, Supervision. **J.M.C. Mol:** Conceptualization, Writing - review & editing, Supervision.

Declaration of Competing Interest

The authors declare that they have no Conflict of interest.

Acknowledgments

This work is part of the research program Understanding Processes using Operando Nanoscopy (UPON) with project number 14205 (B2), which is financed by Nederlandse Organisatie voor Wetenschappelijk Onderzoek (NWO) and partly by AkzoNobel. Besides, T.R. de Kruijff, E. Grafhorst, M. Ahmadi, J. Li, and Z. Yue who were involved in UPON projects A1 and A2 are acknowledged for developing the TEM holders and liquid chips in Prof. Zandbergen's group.

Appendix A. Supplementary data

Supplementary material related to this article can be found, in the online version, at doi:https://doi.org/10.1016/j.corsci.2020.108912.

References

[1] N.E. Prasad, R.J. Wanhill, Aerospace Materials and Material Technologies, Springer, 2017.
[2] J. Chen, E. Costan, M. Van Huis, Q. Xu, H. Zandbergen, Atomic pillar-based nanoprecipitates strengthen AlMgSi alloys, Science 312 (2006) 416–419.
[3] A. Guinier, Structure of age-hardened aluminium-copper alloys, Nature 142 (1938) 569–570.
[4] C. Liu, S.K. Malladi, Q. Xu, J. Chen, F.D. Tichelaar, X. Zhuge, H.W. Zandbergen, In-situ STEM imaging of growth and phase change of individual CuAl X precipitates in Al alloy, Sci. Rep. 7 (2017) 1–8.
[5] S.K. Malladi, Q. Xu, M.A. van Huis, F.D. Tichelaar, K.J. Batenburg, E. Yücelen, B. Dubiel, A. Czyrska-Filemonowicz, H.W. Zandbergen, Real-time atomic scale imaging of nanostructural evolution in aluminum alloys, Nano Lett. 14 (2014) 384–389.
[6] G. Preston, Structure of age-hardened aluminium-copper alloys, Nature 142 (1938) 570-570.
[7] A.E. Hughes, N. Birbilis, J.M. Mol, S.J. Garcia, X. Zhou, G.E. Thompson, High strength Al-alloys: microstructure, corrosion and principles of protection, Recent Trends in Processing and Degradation of Aluminium Alloys 1 (2011).
[8] P.V. Liddicoat, X.-Z. Liao, Y. Zhao, Y. Zhu, M.Y. Murashkin, E.J. Lavernia, R.Z. Valiev, S.P. Ringer, Nanostructural hierarchy increases the strength of aluminium alloys, Nat. Commun. 1 (2010) 1–7.
[9] G. Frankel, WR whitney award lecture: the effects of microstructure and composition on Al alloy corrosion, Corrosion 71 (2015) (2015) 1308–1320.
[10] Z.C. Petrović, Catastrophes caused by corrosion, Vojnoteh. Glas. 64 (2016) 1048–1064.
[11] J. Erlebacher, M.J. Aziz, A. Karma, N. Dimitrov, K. Sieradzki, Evolution of nanoporosity in dealloying, Nature 410 (2001) 450–453.
[12] J. Snyder, K. Livi, J. Erlebacher, Dealloying silver/gold alloys in neutral silver nitrate solution: porosity evolution, surface composition, and surface oxides, J. Electrochem. Soc. 155 (2008) C464–C473.
[13] N. Dimitrov, J. Mann, M. Vukmirovic, K. Sieradzki, Dealloying of Al_2CuMg in alkaline media, J. Electrochem. Soc. 147 (2000) 3283.
[14] S. Lebouil, J. Tardelli, E. Rocca, P. Volovitch, K. Ogle, Dealloying of Al_2Cu, Al_7Cu_2Fe, and Al_2CuMg intermetallic phases to form nanoparticulate copper films, Mater. Corros. 65 (2014) 416–424.
[15] J. Snyder, P. Asanithi, A.B. Dalton, J. Erlebacher, Stabilized nanoporous metals by dealloying ternary alloy precursors, Adv. Mater. 20 (2008) 4883–4886.
[16] Q. Chen, K. Sieradzki, Mechanisms and morphology evolution in dealloying, J. Electrochem. Soc. 160 (2013) C226–C231.
[17] A. Boag, A. Hughes, A. Glenn, T. Muster, D. McCulloch, Corrosion of AA2024-T3 part I: localised corrosion of isolated IM particles, Corros. Sci. 53 (2011) 17–26.
[18] R. Buchheit, A compilation of corrosion potentials reported for intermetallic phases in aluminum alloys, J. Electrochem. Soc. 142 (1995) 3994.
[19] C. Örnek, C. Leygraf, J. Pan, Real-time corrosion monitoring of aluminum alloy using scanning kelvin probe force microscopy, J. Electrochem. Soc. 167 (2020) 081502.
[20] N. Birbilis, R. Buchheit, Investigation and discussion of characteristics for intermetallic phases common to aluminum alloys as a function of solution pH, J. Electrochem. Soc. 155 (2008) C117.
[21] N. Birbilis, R.G. Buchheit, Electrochemical characteristics of intermetallic phases in aluminum alloys: an experimental survey and discussion, J. Electrochem. Soc. 152 (2005) B140.
[22] Y. Zhu, G. Frankel, Effect of major intermetallic particles on localized corrosion of AA2060-T8, Corrosion 75 (2019) 29–41.
[23] Y. Zhu, K. Sun, G. Frankel, Intermetallic phases in aluminum alloys and their roles in localized corrosion, J. Electrochem. Soc. 165 (2018) C807–C820.
[24] Y. Zhu, K. Sun, J. Garves, L.G. Bland, J. Locke, J. Allison, G. Frankel, Micro-and nano-scale intermetallic phases in AA2070-T8 and their corrosion behavior, Electrochim. Acta 319 (2019) 634–648.
[25] A. Boag, R. Taylor, T. Muster, N. Goodman, D. McCulloch, C. Ryan, B. Rout, D. Jamieson, A. Hughes, Stable pit formation on AA2024-T3 in a NaCl environment, Corros. Sci. 52 (2010) 90–103.
[26] G. Frankel, Pitting corrosion of metals: a review of the critical factors, J. Electrochem. Soc. 145 (1998) 2186.
[27] A.E. Hughes, R. Parvizi, M. Forsyth, Microstructure and corrosion of AA2024, Corros. Rev. 33 (2015) 1–30.
[28] R. Buchheit, M. Martinez, L. Montes, Evidence for Cu ion formation by dissolution and dealloying the Al_2CuMg intermetallic compound in rotating ring-disk collection experiments, J. Electrochem. Soc. 147 (2000) 119–124.
[29] N. Dimitrov, J. Mann, K. Sieradzki, Copper redistribution during corrosion of aluminum alloys, J. Electrochem. Soc. 146 (1999) 98.
[30] N. Wint, Z. Barrett, G. Williams, H. McMurray, The study of AA2024 de-alloying using luminol electrogenerated chemiluminescence imaging, J. Electrochem. Soc. 166 (2019) C3417.
[31] F. Renner, A. Stierle, H. Dosch, D. Kolb, T.-L. Lee, J. Zegenhagen, Initial corrosion observed on the atomic scale, Nature 439 (2006) 707–710.
[32] P.J. Denissen, A.M. Homborg, S.J. Garcia, Interpreting electrochemical noise and monitoring local corrosion by means of highly resolved spatiotemporal real-time optics, J. Electrochem. Soc. 166 (2019) C3275.
[33] L. Lacroix, L. Ressier, C. Blanc, G. Mankowski, Combination of AFM, SKPFM, and SIMS to study the corrosion behavior of S-phase particles in AA2024-T351, J. Electrochem. Soc. 155 (2008) C131–C137.
[34] R. Parvizi, A.E. Hughes, M.Y. Tan, R.K. Marceau, M. Forsyth, P. Cizek, A.M. Glenn, Probing corrosion initiation at interfacial nanostructures of AA2024-T3, Corros. Sci. 116 (2017) 98–109.
[35] O. Schneider, G. Ilevbare, J. Scully, R. Kelly, In situ confocal laser scanning microscopy of AA 2024-T3 corrosion metrology II. Trench formation around particles, J. Electrochem. Soc. 151 (2004) B465–B472.
[36] J. Xiao, S. Chaudhuri, Predictive modeling of localized corrosion: an application to aluminum alloys, Electrochim. Acta 56 (2011) 5630–5641.
[37] L. Yin, Y. Jin, C. Leygraf, N. Birbilis, J. Pan, Numerical simulation of micro-galvanic corrosion in Al alloys: effect of geometric factors, J. Electrochem. Soc. 164 (2017) C75–C84.
[38] T.H. da Silva, E.B. Nelson, I. Williamson, C.M. Efaw, E. Sapper, M.F. Hurley, L. Li, First-principles surface interaction studies of aluminum-copper and aluminum-copper-magnesium secondary phases in aluminum alloys, Appl. Surf. Sci. 439 (2018) 910–918.
[39] N. De Jonge, F.M. Ross, Electron microscopy of specimens in liquid, Nat. Nanotechnol. 6 (2011) 695.
[40] F.M. Ross, Opportunities and challenges in liquid cell electron microscopy, Science 350 (2015).
[41] P. Abellan, T. Moser, I.T. Lucas, J. Grate, J. Evans, N. Browning, The formation of cerium (iii) hydroxide nanoparticles by a radiation mediated increase in local pH, RSC Adv. 7 (2017) 3831–3837.
[42] T. Woehl, P. Abellan, Defining the radiation chemistry during liquid cell electron microscopy to enable visualization of nanomaterial growth and degradation dynamics, J. Microsc. 265 (2017) 135–147.
[43] T.J. Woehl, K.L. Jungjohann, J.E. Evans, I. Arslan, W.D. Ristenpart, N.D. Browning, Experimental procedures to mitigate electron beam induced artifacts during in situ fluid imaging of nanomaterials, Ultramicroscopy 127 (2013) 53–63.
[44] N.M. Schneider, Electron beam effects in liquid cell TEM and STEM, in: F.M. Ross (Ed.), Liquid Cell Electron Microscopy, Cambridge University Press, Cambridge, 2016, pp. 140–163.
[45] S.W. Chee, M.G. Burke, Applications of liquid cell TEM in corrosion science, in:

F.M. Ross (Ed.), Liquid Cell Electron Microscopy, Cambridge University Press, Cambridge, 2016, pp. 258–275.
[46] A. Kosari, H. Zandbergen, F. Tichelaar, P. Visser, H. Terryn, A. Mol, Application of in situ liquid cell transmission Electron microscopy in corrosion studies: a critical review of challenges and achievements, Corrosion 76 (2020) 4–17.
[47] S.W. Chee, D.J. Duquette, F.M. Ross, R. Hull, Metastable structures in Al thin films prior to the onset of corrosion pitting as observed using liquid cell transmission electron microscopy, Microsc. Microanal. 20 (2014) 462–468.
[48] S.W. Chee, J.-H. Park, A. Pinkowitz, B. Engler, F.M. Ross, D. Duquette, R. Hull, Liquid cell TEM of Al thin film corrosion under potentiostatic polarization, Microsc. Microanal. 21 (2015) 973–974.
[49] S.W. Chee, S.H. Pratt, K. Hattar, D. Duquette, F.M. Ross, R. Hull, Studying localized corrosion using liquid cell transmission electron microscopy, Chem. Commun. 51 (2015) 168–171.
[50] J.W. Key, S. Zhu, C.M. Rouleau, R.R. Unocic, Y. Xie, J. Kacher, Investigating local oxidation processes in Fe thin films in a water vapor environment by in situ liquid cell TEM, Ultramicroscopy 209 (2020) 112842.
[51] X.L. Zhong, S. Schilling, N.J. Zaluzec, M.G. Burke, Sample preparation methodologies for in situ liquid and gaseous cell analytical transmission electron microscopy of electropolished specimens, Microsc. Microanal. 22 (2016) 1350–1359.
[52] S.C. Hayden, C. Chisholm, R.O. Grudt, J.A. Aguiar, W.M. Mook, P.G. Kotula, T.S. Pilyugina, D.C. Bufford, K. Hattar, T.J. Kucharski, Localized corrosion of low-carbon steel at the nanoscale, Npj Mater. Degrad. 3 (2019) 1–9.
[53] R. Buchheit, R. Grant, P. Hlava, B. McKenzie, G. Zender, Local dissolution phenomena associated with S phase (Al_2CuMg) particles in aluminum alloy 2024-T3, J. Electrochem. Soc. 144 (1997) 2621.
[54] T. Hashimoto, X. Zhang, X. Zhou, P. Skeldon, S. Haigh, G. Thompson, Investigation of dealloying of S phase (Al_2CuMg) in AA 2024-T3 aluminium alloy using high resolution 2D and 3D electron imaging, Corros. Sci. 103 (2016) 157–164.
[55] M. Vukmirovic, N. Dimitrov, K. Sieradzki, Dealloying and corrosion of Al alloy 2024 T3, J. Electrochem. Soc. 149 (2002) B428–B439.
[56] J. Wang, B. Zhang, Y. Zhou, X. Ma, Multiple twins of a decagonal approximant embedded in S-Al_2CuMg phase resulting in pitting initiation of a 2024Al alloy, Acta Mater. 82 (2015) 22–31.
[57] X. Zhang, T. Hashimoto, J. Lindsay, X. Zhou, Investigation of the de-alloying behaviour of θ-phase (Al_2Cu) in AA2024-T351 aluminium alloy, Corros. Sci. 108 (2016) 85–93.
[58] N. de Jonge, Theory of the spatial resolution of (scanning) transmission electron microscopy in liquid water or ice layers, Ultramicroscopy 187 (2018) 113–125.
[59] S. Keskin, P. Kunnas, N. de Jonge, Liquid-phase electron microscopy with controllable liquid thickness, Nano Lett. 19 (2019) 4608–4613.
[60] A. Boag, A. Hughes, N. Wilson, A. Torpy, C. MacRae, A. Glenn, T. Muster, How complex is the microstructure of AA2024-T3? Corros. Sci. 51 (2009) 1565–1568.
[61] P. Yu, S.A. Hayes, T.J. O'Keefe, M.J. O'Keefe, J.O. Stoffer, The phase stability of cerium species in aqueous systems: II. The systems. Equilibrium considerations and pourbaix diagram calculations, J. Electrochem. Soc. 153 (2005) C74.
[62] L. Paussa, F. Andreatta, D. De Felicis, E. Bemporad, L. Fedrizzi, Investigation of AA2024-T3 surfaces modified by cerium compounds: a localized approach, Corros. Sci. 78 (2014) 215–222.
[63] K.A. Yasakau, M.L. Zheludkevich, S.V. Lamaka, M.G. Ferreira, Mechanism of corrosion inhibition of AA2024 by rare-earth compounds, J. Phys. Chem. B 110 (2006) 5515–5528.